Energy Technology
Generation, Conversion, Storage, Distribution
www.entechnol.de

Check for updates

Three-Dimensional Numerical Simulations on the Effect of Particle Porosity of Lithium-Nickel–Manganese–Cobalt–Oxide on the Performance of Positive Lithium-Ion Battery Electrodes

Susanne Cernak, Florian Schuerholz, Michael Kespe, and Hermann Nirschl*

A spatially resolved electrochemical model is applied to single porous lithium–nickel–manganese–cobalt-oxide (NMC) particles to evaluate the effect of particle porosity on the half-cell performance. The arrangement of the primary particles within the investigated secondary particles is computer-generated by means of the Fibonacci lattice method and is therefore identical. By varying the thickness of the sintering bridges between the primary particles, the different particle porosities are obtained. The numerical results reveal that transport limitations decrease with increasing particle porosity. This becomes evident in lower local overpotentials and more homogeneous lithium concentrations in the solid, leading to higher utilizable capacities. To find optimum particle porosities for different load conditions, a utility value analysis of two assessment approaches is performed. The volume-based evaluation shows that nonporous particles are most suitable for high-energy applications $\ll$1 C, whereas for medium to high-power applications (1 to 10 C), particles with porosities between 10% and 20% perform best. Interestingly, the latter show even higher utilizable energy densities compared with the nonporous and the highly porous particles. In contrast to that, the gravimetric results show that the electrochemical performance increases with the particle porosity. Thus, the optimum inner porosity of NMC particles depends on the desired application.

1. Introduction

Ranging from lightweight portable and mobile devices, to electric vehicles as well as stationary energy stores, lithium-ion batteries (LIBs) have become part of almost all areas of everyday life.[1] Compared to other battery technologies, LIBs are advantageous concerning energy density and performance. Through a high level of research, LIBs have been and are constantly being improved in terms of their cycle stability and aging resistance.[2,3] Nevertheless, the demand for even more powerful mobile energy storage systems is increasing. For this reason, research groups around the world are focusing on improving LIBs, with the aim of achieving ever-higher energy and power densities, improved cycle stability and minimizing manufacturing costs, while maintaining safety aspects.[3]

LIBs consist of anode and cathode layers, which are electrically insulated by a separator, but are ionically conductively connected. The two electrode layers have a complex, particulate structure on the nano- and micrometer scale and the pore space is filled with an electrolyte.[4] Regardless of the size and shape of the battery, the performance-determining transport processes are located on the particle or sub-particle level and are experimentally accessible only with considerable metrological effort. In this context, detailed spatially resolved numerical simulations can contribute to a profound understanding of the transport processes within a LIB.[5]

In 2005, García et al.,[6] conducted one of the first physics-based electrochemical simulations of a LIB on fully resolved electrode microstructures in 2D. Following this approach, 3D simulations were performed using spherical or other idealized particles[7–10] or microstructures reconstructed from focused ion beam–scanning electron microscopy (FIB-SEM) and μCT images.[5,11] The latter showed that the real particle morphology deviates strongly from the spherical shape. This leads to local fluctuations, which cannot be represented by an idealized microstructure.[5,12]

Lithium–nickel–manganese–cobalt-oxide (NMC) is the most widespread cathode active material (AM) on the battery market according to the current state of the art.[3] Nevertheless, there are some challenges regarding NMC cathodes, such as the low solid-state diffusivity and a not very satisfactory thermal stability, which was found to need improvement.[13] There are several

S. Cernak, F. Schuerholz, Dr. M. Kespe, Prof. H. Nirschl
Institute of Mechanical Process Engineering and Mechanics
Karlsruhe Institute of Technology
Strasse am Forum 8, 76131 Karlsruhe, Germany
E-mail: susanne.cernak@kit.edu

The ORCID identification number(s) for the author(s) of this article can be found under https://doi.org/10.1002/ente.202000676.

© 2020 The Authors. Energy Technology published by Wiley-VCH GmbH. This is an open access article under the terms of the Creative Commons Attribution License, which permits use, distribution and reproduction in any medium, provided the original work is properly cited.

The copyright line for this article was changed on 17 December 2020 after original online publication.

DOI: 10.1002/ente.202000676

ways to modify cathode materials in terms of thermal, mechanical, and chemical stability. On the one hand, this is achieved by varying the chemical composition[14], on the other hand, by optimizing the AM particle morphology.[15] Uddin et al.[15] stated that nanotechnology shows new ways to overcome transport-related capacity limitations in the cathode material and thereby increase the performance of batteries. This can be realized by a suitable particle morphology or 3D nanostructures that ensure reduced solid-state diffusion lengths in the AM. Furthermore, this leads to lower transport resistances and faster intercalation and deintercalation reactions.[15–21] Shaju and Bruce[22] synthesized macroporous NMC and obtained a very cycle-resistant material, which showed good performance characteristics even at elevated temperatures around 50 °C.[22] Dreizler et al.[23] refined commercially available NMC material and generated highly porous NMC particles with porosities exceeding 40%. Compared to the commercial nonporous AM particles with less than 4% inner porosity, the highly porous AM particles showed a better fast-charging capability, a higher available capacity, and a better mechanical stability.[23] Lueth et al.[24] modeled porous NMC via the volume averaging technique and implemented the equations in an extended Newman model. They observed lower transport losses and higher discharge capacities of the porous AM particles.[24] Furthermore, in a previous contribution, 3D and spatially resolved simulations were carried out to determine the influence of NMC primary and secondary particle sizes on the electrochemical performance of LIB half-cells.[25]

This publication continues the research on the influence of particle morphology and investigates the impact of the particle porosity of NMC AM on the electrochemical performance of LIBs by systematic spatially resolved simulations. At the manufacturing of LIBs many processing steps occur, which influence the ionic and electronic transport behavior in the assembled batteries to a large extent.[26] In this contribution, the pure AM response on the different load conditions is of interest. Therefore, single particle simulations are conducted. This gives insight into the capacity-limiting transport processes involved and reveals the origin of the differences in the utilizable energy and power density of the various porous particles.

2. Electrode Particle Generation

For the investigation of the influence of different porous AM particles on the electrochemical performance, a computer-aided generation of secondary AM particles with a defined primary particle arrangement and virtual sintering is applied. Experimental investigations show that commercial NMC particles typically have primary particles in the range between 0.2 and 3.6 μm and a volume-related mean diameter $d_{50,3}$ of the secondary particles between 8 and 12 μm.[23,27,28] Thus, a primary particle diameter of 1 μm and a secondary particle diameter of 10 μm is used for the particle generation. To be able to compare the results and to keep other influencing effects constant, single secondary particle simulations with identical primary particle arrangement but different thicknesses of the sintering bridges are used.

The calculation of an approximately equal distribution of primary particles on the respective shell layer S_X is performed using the Fibonacci lattice method. The angle Φ_{Xi} of each primary particle i on the shell S_X is the azimuthal angle of the spherical coordinates with values between 0 and 2π and is given in Equation (1). The golden section $((1+\sqrt{5}))/2$ serves as the basis for the Fibonacci numbers, which is why this approach is called the Fibonacci lattice method.[29]

$$\theta_{Xi} = 2\pi \cdot \frac{(1+\sqrt{5})}{2} \cdot (i - 0.5) \tag{1}$$

The angle φ_{Xi} is the pole angle of the spherical coordinates and can take values between 0 (north pole) and π (south pole). It is calculated in Equation (2) using the consecutive primary particle index $i = \{1, ..., n_X\} \in \mathbb{N}$ for each shell S_X and the total number of spheres in the respective shell n_X.[29]

$$\varphi_{Xi} = \cos^{-1}\left(1 - \frac{2 \cdot (i - 0.5)}{n_X}\right) \tag{2}$$

The sphere count n_X results from geometrical considerations. The overall number of primary particles for one porous secondary particle with a diameter of 10 μm and a primary particle diameter of 1 μm with a maximum shell count of $N = 5$ amounts to $n_P = 522$. Further geometrical properties of the regarded AM particles are summarized in **Table 1**. For simplification, the particles are named according to their inner porosity.

As expected, the geometry with the highest porosity has the largest active surface area A. However, the solid volume V of the respective particles decreases linearly with increasing porosity, starting with the reference particle with 0% porosity (see Table 1). It can be seen from Table 1 that the volume-specific surface area S_V, increases almost linearly with increasing porosity of the particles. A schematic representation of the electrode particle set-up is shown in **Figure 1**.

3. Electrochemical Model

The underlying model considers the charge and species transport in 3D spatially resolved electrochemical half-cells, with one solid electrode region and a liquid electrolyte region coexisting as two nonoverlapping subdomains.[10] The focus in this contribution lies on the simulation of the positive electrode. Hence, the anode is not resolved, but assumed to consist of metallic lithium and is modeled by a suitable boundary condition.

The charge conservation equation in Equation (3) is used, to describe the electron conduction in the porous NMC particle.

Table 1. Properties of the investigated porous AM particles.

Porosity, ε [%]	Solid volume, V [μm^3]	Active surface area, A [μm^2]	Volume-specific surface area, S_V [μm^{-1}]	Specific surface area [m^2 g^{-1}]
40.4	278.71	1419.97	5.09	1.08
30.3	325.98	1266.35	3.88	0.87
20.0	373.99	1036.54	2.77	0.59
11.6	413.47	747.32	1.81	0.38
5.5	441.97	541.20	1.22	0.26
0.0	467.66	337.56	0.72	0.15

© 2020 The Authors. Energy Technology published by Wiley-VCH GmbH

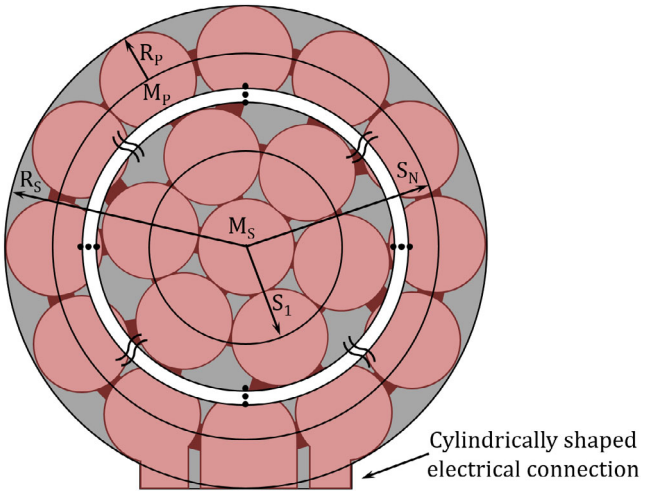

Figure 1. Schematic representation of the computer-generated porous particles using the Fibonacci lattice method. The basic particle structure was created by means of a shell-shaped arrangement (black circles $S_1 \ldots S_N$) of the equally sized primary particles with radius R_P and their approximately equally distributed centers M_P on the respective shells (reddish circles). By "virtual sintering" of the primary particles, the different porosities can be adjusted by variable filling of the pore spaces (dark red compounds), whereby the secondary particle radius R_S remains constant. For an ideal connection of the particles to the current collector, the particles have a cylinder-shaped electrical connection part on the bottom side.

Here ϕ_S represents the electrical potential and κ_S the electrical conductivity.

$$\nabla \cdot (\kappa_S \cdot \nabla \phi_S) = 0 \tag{3}$$

As shown in Equation (4), the lithium transport in the AM particles is modeled via solid-state diffusion. In this context, c_S represents the lithium concentration and D_S the solid-state diffusion coefficient of lithium. In the scope of this contribution, only isotropic transport properties are considered.

$$\frac{\partial c_S}{\partial t} = \nabla \cdot (D_S \cdot \nabla c_S) \tag{4}$$

The liquid electrolyte is modeled using concentrated solution theory, while charge neutrality is presumed (see Equation (5)).[30,31] In Equation (5), c_E stands for the lithium concentration, D_E for the diffusion coefficient of lithium and $\vec{i}_E$ for the ionic current density in the electrolyte. The indicator for the mobility of lithium-ions in the electrolyte is the transference number t_+^0 and F represents the Faraday constant.

$$\frac{\partial c_E}{\partial t} = \nabla \cdot \left(D_E \cdot \nabla c_E + \frac{\vec{i}_E t_+^0}{F} \right) \tag{5}$$

$$\vec{i}_E = -\kappa_E \cdot \nabla \phi_E + \frac{2\Re T \kappa_E}{F}(1 - t_+^0) \nabla \ln(c_E) \tag{6}$$

In Equation (6), ϕ_E represents the electrical potential of the electrolyte and $\Re$ the universal gas constant. Furthermore, κ_E is the ionic conductivity and T the absolute temperature. To couple the solid electrode and the electrolyte, a Butler–Volmer-type electrochemical kinetics condition is used (see Equation (7)).[30,32,33] As shown in Equation (7), the exchange current density $\vec{i}_{BV}$ depends on the material-specific kinetic constant k_{BV}, the concentrations of the electrolyte c_E and AM c_S at the particle surface $\Gamma_{S,E}$ and the maximum stoichiometric lithium concentration of NMC $c_{S,max}$. The overpotential is indicated by η and the anodic or cathodic apparent transfer coefficient by α_a or α_c, respectively.[30]

$$\vec{i}_{BV} = k_{BV} \cdot \left(c_{S,max} - c_S|_{\Gamma_{S,E}} \right)^{\alpha_a} \cdot \left(c_S|_{\Gamma_{S,E}} \right)^{\alpha_c} \cdot \left(c_E|_{\Gamma_{S,E}} \right)^{\alpha_a} \cdot \left[\exp\left(\frac{\alpha_a F \eta}{\Re T} \right) - \exp\left(-\frac{\alpha_c F \eta}{\Re T} \right) \right] \tag{7}$$

According to Equation (8), the overpotential η is calculated from the difference between the electrical potentials of the electrode ϕ_S as well as the electrolyte ϕ_E on the particles' surface and the material-specific, concentration-dependent equilibrium potential $U_{eq}(c_S)$.

$$\eta = \phi_S|_{\Gamma_{S,E}} - \phi_E|_{\Gamma_{S,E}} - U_{eq}\left(c_S|_{\Gamma_{S,E}} \right) \tag{8}$$

In Equation (9), the continuity condition is stated. This means that the ionic current density $\vec{i}_E$ at the active surface from the electrolyte side with normal vector $\vec{n}_E$ has to be equal to the intercalation current density $\vec{i}_{BV}$ at the active surface from the particles side into the AM with normal vector $\vec{n}_S$. Note that $\vec{n}_S$ points in the opposite direction of $\vec{n}_E$.

$$\vec{i}_{BV}|_{\Gamma_{S,E}} \cdot \vec{n}_S = -\vec{i}_E|_{\Gamma_{S,E}} \cdot \vec{n}_E \tag{9}$$

As the electrochemical reactions at the surface of the lithium metal anode are assumed to be fast, the electrical potential at the anode is set to 0 V. Furthermore, the absolute ionic current at the anode is equal to the electric current at the cathode current collector, to satisfy the charge conservation condition over the entire half-cell. The ionic current density at the cathode current collector Γ_{CC} is $\vec{i}_E|_{\Gamma_{CC}} \cdot \vec{n}_E = 0\,\mathrm{A\,m^{-2}}$ in normal direction, because it is impermeable to lithium ions. The material-specific model parameters that are used throughout this contribution are summarized in **Table 2**.

Figure 2 shows a diagonally cut simulation setup and result of the $\varepsilon = 11.6\%$ geometry. From this figure, it can be seen that the cases are configured as half-cells with an AM particle as positive electrode. The porous particle is assumed to be ideally connected to the cathode current collector and the vertical electrolyte boundaries are periodically connected. The anode is assumed to consist of metallic lithium and is modeled by a suitable boundary condition. The assumption of isothermal operation at $T = 298\,\mathrm{K}$ applies. For the initialization of the cases homogeneous lithium distributions within the solid $c_{S,ref}$ and the electrolyte $c_{E,ref}$ are used. Furthermore, the potential at which the simulations start is $\phi_{S,ref} = 4.2\,\mathrm{V}$.

For the concentration dependent equilibrium potential of NMC $U_{eq}(c_S)$, a correlation published by Stewart et al. and Kindermann et al. is used, which is shown in Equation (10).[32,33]

© 2020 The Authors. Energy Technology published by Wiley-VCH GmbH

Table 2. Material properties of NMC, electrolyte, and Butler–Volmer kinetics.

	Value	Unit	Reference
Parameters of cathode material			
Electrical conductivity κ_S	10	S m^{-1}	[40]
Coefficient of diffusion D_S	3.5×10^{-15}	m^2 s^{-1}	[41]
Solid density of NMC ρ_{NMC}	4700	kg m^{-3}	[28,35]
Solid density of carbon black ρ_{CB}	2200	kg m^{-3}	[35]
Solid density of PVDF binder ρ_{PVDF}	1800	kg m^{-3}	[42]
Cathode coating porosity ϵ_C	0.35	–	[35,43]
Lithium concentration with equilibrium initial condition at 4.2 V $c_{S,ref}$	21 736	mol m^{-3}	[33]
Maximum stoichiometric lithium concentration $c_{S,max}$	51 385	mol m^{-3}	[44]
Equilibrium potential U_{eq} of NMC	$f(c_S)$	V	see (10)[32,33]
Parameters of electrolyte			
Ionic conductivity κ_E	$f(c_E)$	S m^{-1}	see (11)[8]
Transference number t_+^0	0.4	–	[8]
Coefficient of diffusion D_E	$f(c_E)$	m^2 s^{-1}	see (12)[8]
Initial lithium concentration $c_{E,ref}$	1000	mol m^{-3}	[10]
Parameters of Butler–Volmer kinetics			
Cathodic apparent transfer coefficient α_c	0.5	–	[45]
Anodic apparent transfer coefficient α_a	0.5	–	[45]
Butler–Volmer reaction rate constant k_{BV}	2.895×10^{-7}	A m mol^{-1}	[33]

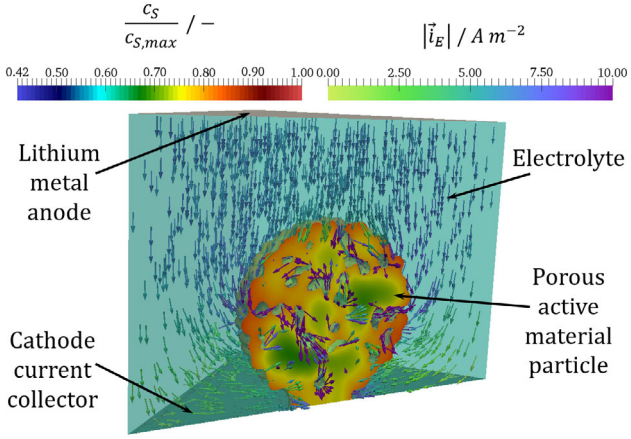

Figure 2. Simulation case setup for the single porous secondary particle simulations. Here the lithium concentration in the $\varepsilon = 11.6\%$ particle and the ionic current densities in the electrolyte are shown. The arrows represent the ionic current density in the electrolyte region. The coloring was adopted to be able to show the differences in the free electrolyte, therefore the ionic current densities in the pore space is up to 100 times higher than in the electrolyte surrounding the particle.

$$U_{eq} = 6.0826 - 6.9922 \cdot c_S + 7.1062 \cdot {c_S}^2 - 0.54549 \cdot 10^{-4} \cdot \exp(124.23 \cdot c_S - 114.2593) - 2.5947 \cdot {c_S}^3 \quad (10)$$

The dependence of the ionic conductivity κ_E of the electrolyte on its local lithium concentration c_E is captured in Equation (11) by means of the correlation proposed by Less et al.[8]

$$\kappa_E = -2.39 \cdot 10^{-11} c_E^4 + 1.21 \cdot 10^{-7} c_E^3 - 2.89 \cdot 10^{-4} c_E^2 + 0.32 c_E - 2.789 \quad (11)$$

To account for the concentration dependent electrolyte diffusion coefficient D_E, a correlation fitted by Kespe et al.[9] to the published data of Less et al.[8] is used (see Equation (12)). Here, the electrolyte concentration c_E is in mol m^{-3}.

$$D_E = 1.2 \cdot 10^{-21} c_E^4 - 6.5 \cdot 10^{-18} c_E^3 + 1.14 \cdot 10^{-14} c_E^2 - 8.06 \cdot 10^{-12} c_E + 2.24 \cdot 10^{-9} \quad (12)$$

For the comparison of the numerical results, the depth of discharge (DOD) is an important battery parameter. The DOD indicates how much of the theoretical maximum capacity of the battery can be used under the prevailing operating conditions. In the spatially resolved model, this quantity is given for the electrode domain Ω_S by Equation (13).[10]

$$\mathrm{DOD} = 1 - \frac{\int (c_S(\vec{x}, t) - c_{S,ref}) \mathrm{d}\Omega_S}{\int (c_{S,max} - c_{S,ref}) \mathrm{d}\Omega_S} \quad (13)$$

To determine the performance of a simulated battery half-cell, the "utilizable capacity" (UC) is adduced and is calculated as shown in Equation (14).[10]

$$\mathrm{UC} = \frac{\mathrm{DOD(COV)}}{\mathrm{DOD_{eq}(COV)}} \cdot 100 \quad (14)$$

In this context, the terminal voltage also referred to as cut-off voltage (COV), which is set to COV = 3.25 V in this contribution.

© 2020 The Authors. Energy Technology published by Wiley-VCH GmbH

The charge or discharge rate of a battery or battery half-cell is called C-rate.[34] The C-rate is used to make different types of batteries and materials comparable with one another. It is defined as the constant current that is necessary to fully charge or discharge the half-cell, times the value of the C-rate within 1 h. In Equation (15), $\overline{i_{\mathrm{BV}}}$ stands for the mean intercalation current density, A represents the AM particle surface area, and V the solid particle volume.

$$\text{C–rate} = \frac{3600\,\frac{s}{h} \cdot \overline{i_{\mathrm{BV}}} \cdot A}{\mathrm{F} \cdot (c_{\mathrm{S,max}} - c_{\mathrm{S,ref}}) \cdot V} \tag{15}$$

To evaluate the performance capability of the NMC particles with different porosities, the measuring quantities "utilizable energy density" (UED) and "utilizable power density" (UPD) are used. Therefore, the results of the single-particle simulations are transferred to the macroscopic "bulk" level using two different approaches. At first a gravimetric approach is used, in which the results are transferred to the same mass of AM. For this consideration, it should be noted that the particles with a higher inner porosity occupy a larger overall volume than those with lower porosity. The values associated with this approach receive the index MB, which stands for "mass-based".

For the second, "the volumetric", approach, a reference cathode slurry composition of Landesfeind et al.[35] is used to obtain the number of AM particles within $1\,\mathrm{m}^3$ of cathode slurry. As this approach refers to the enveloping volume of the particles, which is identical for the particles investigated here, the number of AM particles in $1\,\mathrm{m}^3$ slurry remains constant. The values, which refer to this approach, are given the index VB for "volume-based".

Both approaches imply the assumptions that the single secondary particle behavior is dominant also on the macroscopic level. Furthermore, it is assumed that the considered macroscopic AM quantity is composed exclusively of particles of the same size and morphological properties. In addition, the assumption of an ideal and uniform electronic and ionic connection of the particles applies. Moreover, other influences, which might interfere with the electrochemical performance of the pure AM, i.e., lithium-consuming side reactions, electrolyte decomposition, etc. are neglected.

The calculation of the number of NMC particles N_{VB} in a cubic meter of cathode slurry is done with the help of a representative composition published by Landesfeind et al.[35] It consists of the following mass fractions w: $w_{\mathrm{NMC}} = 0.96$, $w_{\mathrm{CB}} = 0.02$ and $w_{\mathrm{PVDF}} = 0.02$. In Equation (16), the volume fraction of NMC φ_{NMC} in the solid phase is calculated using the respective solid densities ρ, which are given in Table 2.

$$\varphi_{\mathrm{NMC}} = \frac{\frac{w_{\mathrm{NMC}}}{\rho_{\mathrm{NMC}}}}{\frac{w_{\mathrm{NMC}}}{\rho_{\mathrm{NMC}}} + \frac{w_{\mathrm{CB}}}{\rho_{\mathrm{CB}}} + \frac{w_{\mathrm{PVDF}}}{\rho_{\mathrm{PVDF}}}} = 0.91 \tag{16}$$

The number of secondary particles is given by Equation (17) using the cathode porosity ε_{C}. As the outer shape of the AM particles is identical, the nonporous particle is used as reference volume with $V_{0\%}$.

$$N_{\mathrm{VB}} = \frac{(1 - \varepsilon_{\mathrm{C}}) \cdot \varphi_{\mathrm{NMC}}}{V_{0\%}} = 1.2648 \times 10^{15}\,\mathrm{m}^{-3} \tag{17}$$

The calculation of the utilizable energy UE_{P} of the respective particles is done using Equation (18). Within the equation, $t(0)$ represents the discharge start time and the time $t(\mathrm{COV})$ when the COV is reached in seconds "s". $\Phi_{\mathrm{S,CC}}(t)$ represents the time-dependent electrical voltage in Volts "V" and $I_{\mathrm{CC}}(t)$ the time-dependent electrical current in Ampere "A", both at the current collector of the cathode. The unit of UE_{P} is Watt seconds "Ws".

$$UE_{\mathrm{P}} = \int_{t(0)}^{t(\mathrm{COV})} \Phi_{\mathrm{S,CC}}(t) \cdot I_{\mathrm{CC}}(t)\mathrm{d}t \tag{18}$$

By multiplying the particle-related value UE_{P} by the volume-specific particle number, the volumetric UED in Watt hours per cubic meter "Wh m^{-3}" is obtained (see Equation (19)).

$$UED_{\mathrm{VB}} = \frac{UE_{\mathrm{P}} \cdot N_{\mathrm{VB}}}{3600\,\frac{s}{h}} \tag{19}$$

For the gravimetric UED in Equation (20), for which the unit is Watt hours per kilogram "Wh kg^{-1}", UE_{P} is divided by the density of solid NMC ρ_{NMC} (see Table 2) and the solid volume V of the differently porous secondary particles (see Table 1).

$$UED_{\mathrm{MB}} = \frac{UE_{\mathrm{P}}}{\rho_{\mathrm{NMC}} \cdot V \cdot 3600\,\frac{s}{h}} \tag{20}$$

The volumetric or gravimetric values for the UPD result from the respective UEDs divided by the discharge time until COV is reached, while x stands either for VB or MB (see Equation (21)). $\mathrm{UPD_{VB}}$ is given in Watt per cubic meter "W m^{-3}" and the unit of $\mathrm{UPD_{MB}}$ is Watt per kilogram "W kg^{-1}".

$$\mathrm{UPD}_x = \frac{\mathrm{UED}_x \cdot 3600\,\frac{s}{h}}{(t(\mathrm{COV}) - t(0))} \tag{21}$$

The model equations were implemented using the finite volume method in the open source simulation platform OpenFOAM of version 6. The simulations were conducted in parallel on the supercomputer ForHLR, located at the Steinbuch Centre for Computing in Karlsruhe.

4. Results and Discussion

Various manufacturers of commercial batteries with nonporous NMC as cathode AM, which are built as 18 650 round cells, specify 2C or 4C as the highest discharge rate in their datasheet.[33] For this reason, a numerical C-rate study ranging from 0.1C to 10C and simulations with the same absolute intercalation current (SAIC) as the 4C of the nonporous particle are conducted. With the help of these simulations, statements about the influence of the particle porosity on the electrochemical performance can be deduced.

Figure 3 shows the half-cell potentials upon galvanostatic discharging at a 4C discharge rate. It can be seen that at higher porosities, the half-cell potential remains at a higher level when

© 2020 The Authors. Energy Technology published by Wiley-VCH GmbH

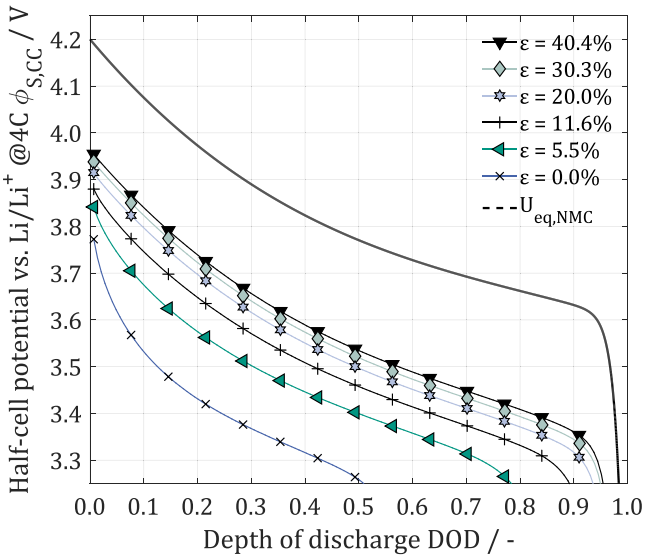

Figure 3. Half-cell potentials of the investigated porous particles for a 4C discharge cycle over the DOD.

comparing at the same DOD. However, it should be considered that at higher porosities, the solid particle volume is smaller and thus the mass as well as the theoretical maximum capacity of the AM particle is lower. For this reason, a smaller absolute intercalation current is present, as the C-rate is proportional $\frac{i_{BV}}{V}$ (see Equation (15)). Furthermore, the active surface area of a porous particle is higher and therefore, the intercalation current density decreases which leads to lower concentration gradients and smaller overpotentials. Thus, the achievable DOD and the UC gain larger values before the COV is reached.

Half-cell potentials represent a macroscopically measurable quantity. To determine the root cause of the shown behavior, first the lithium concentration fields of the electrolyte domain are evaluated. In a second step, the lithium concentration fields of the investigated porous AM particles are analyzed.

As can be seen in Equation (12), the lithium diffusion coefficient in the electrolyte D_E is considered as concentration-dependent and is in the order of $10^{-10}\,m^2\,s^{-1}$. Hence, it is almost five orders of magnitude higher than the solid-state diffusion coefficient of lithium in NMC. For this reason, it is favorable to transport lithium via the electrolyte to the inner part of the AM. However, a depletion of lithium ions in the electrolyte inside the porous particles may occur, especially at elevated C-rates. For this reason, the 10C discharge simulations were examined more closely (see **Figure 4**).

In Figure 4, the center-cut electrolyte domains of the investigated porous particle simulations at the end of the respective 10C galvanostatic discharge cycle are shown. The images show the relative lithium concentration fields in the electrolyte subdomains.

For the highly porous particles with $\varepsilon > 20\%$, the maximum reduction of the electrolyte concentration inside the particle is 1.8%, in comparison to the initial lithium concentration. At a porosity of $\varepsilon = 20\%$, the maximum concentration depletion is around 8.4% and for particles with already very narrow pores ($\varepsilon = 11.6\%$ and $\varepsilon = 5.5\%$), but still with a large internal active surface area, the electrolyte depletion reaches a maximum of 55.1%. However, the electrolyte surrounding the nonporous particle shows no noticeable lithium concentration depletion.

The simulations show that electrolyte depletion is pronounced in regions where lithium ions have to be transported through narrow pore cross-sections, especially when these pores serve as a connector to a large inner surface area of closed pores. Thus, these small pore cross-sections are prone to high ionic current densities. Hence, as according to Latz and Zausch,[31] ionic current densities induce thermal heating, these regions may become hot spots, in which degradation processes and electrolyte decomposition might be pronounced.[36] Therefore, from the electrolyte's view-point, it can be stated that nonporous particles

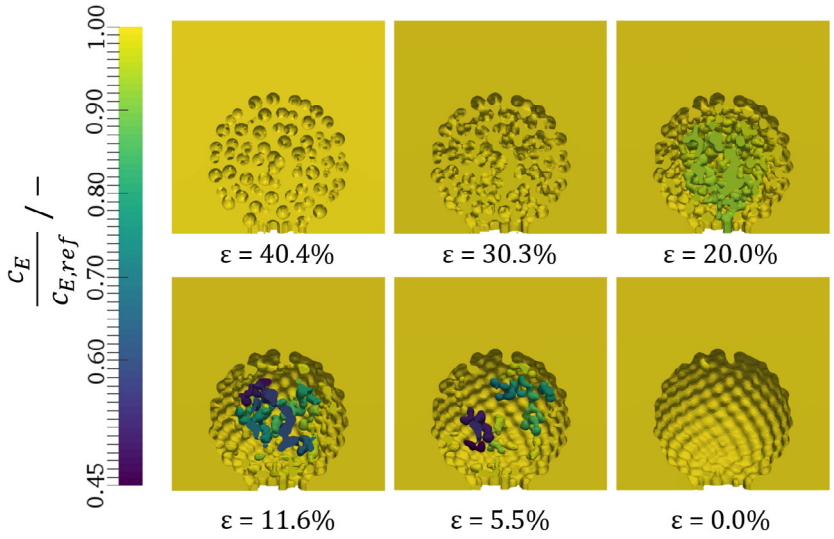

Figure 4. Representation of the relative lithium concentration in the electrolyte subdomains, which are cut at the particles' center and depicted each at the end of a 10C galvanostatic discharge cycle.

© 2020 The Authors. Energy Technology published by Wiley-VCH GmbH

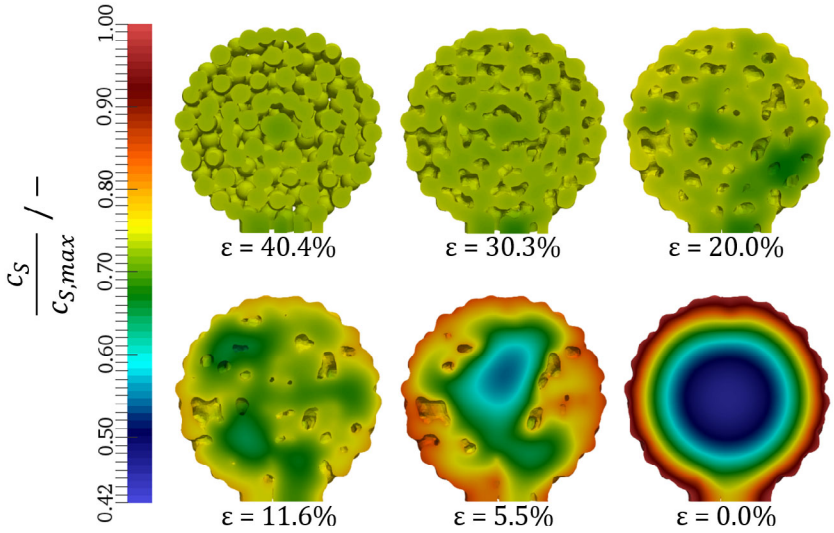

Figure 5. Cross-section through the spatial concentration distribution of the investigated porous AM particles at a galvanostatic discharge of 4C. At the depicted DOD of 0.53, the nonporous particle has already reached the end of its discharge cycle.

or AM particles with an open-pore structure and a porosity $\varepsilon > 20\%$ are advantageous at high discharge rates.

Figure 5 shows the simulated spatial concentration distribution of the investigated porous particles at DOD = 0.53 at a galvanostatic discharge rate of 4C. It can be seen that the highly porous particles are uniformly lithiated. The inhomogeneities of the lithium concentration fields increase with decreasing inner porosity of the particles. At a porosity $\varepsilon \leq 20\%$, the number of closed pores increases, which results in larger solid areas where the lithium can only be transported by means of solid-state diffusion. These areas show a lower lithium concentration and the tendency toward a diffusion-limited state of the respective particles increases. The extreme of the aforementioned is represented by the nonporous particle ($\varepsilon = 0\%$). In the depicted state of operation, it has already reached the maximum lithium concentration at its outer perimeter and therefore its discharge limit (see Figure 5).

The reason for this behavior at constant C-rates is twofold. First, decreasing porosities lead to higher particle-specific capacities and hence to increasing intercalation currents. Second, a decreasing inner particle porosity goes along with a reduced active surface area which leads to increasing intercalation current densities and therefore to higher local overpotentials. In addition to that, the low solid-state diffusion coefficient leads to an increased lithium concentration at the particle surface, which negatively affects the local equilibrium potential. The combination of these effects lead to lower half-cell potentials at decreasing inner particle porosities and hence to decreasing UCs.

When applying the particle-related C-rates, the results reveal that high porosities are favorable for achieving high UCs. However, in this mode of operation, the applied intercalation current is directly proportional to the solid volume or in other words the mass of the particles. For the comparison of the performance of the individual particles with regard to their enveloping volume, in the following, a comparison of the behavior at SAICs is used. This in turn leads to increasing discharge rates for increasing particle porosities. In the following, the total intercalation current of the nonporous particle at a discharge rate of 4C serves as a reference. The transfer of this respective discharge current on the particle with a porosity of $\varepsilon = 40.4\%$ leads to a particle-specific discharge rate of 6.71C.

The cross-section of the dimensionless lithium-concentration fields of the investigated particle structures at an identical discharge time of 480 s is shown in **Figure 6**. Consistent to the aforementioned results, it can be seen that the particles with an inner porosity of $\varepsilon > 20\%$ show a more homogeneous lithium concentration distribution compared to the particles with a lower inner porosity. However, at the depicted time, the overall DOD of the highly porous particles is higher compared to the dense particles (e.g., DOD($\varepsilon = 40\%$) = 0.90 while DOD($\varepsilon = 0\%$) = 0.53), which is due to the increasing discharge rates at increasing particle porosity. Furthermore, it can be seen in Figure 6 that the dense particles are in a diffusion limited state of operation, i.e., not the entire particle capacity can be used at the applied intercalation current. As before, the nonporous particle has already reached the end of its discharge at DOD = 0.53.

The results of Figure 6 show that particles with an increased inner porosity are less prone to solid-state diffusion limitations and therefore allow a high utilization of the AM capacity. However, for a given particle size, an increase in internal porosity is accompanied by a decrease in theoretical capacity. Hence, the question arises, if there is an optimum inner porosity of AM particles. To tackle this question, in the following, the volumetric and gravimetric UEDs and UPDs are used for a quantitative analysis of the numerical results.

In **Figure 7**, the diagram (a) shows volumetric and (b) gravimetric Ragone-representations of the numerically investigated porous secondary particles. This kind of depiction is commonly used in the assessment of battery systems.[37] A quantitative comparison with published data of Winter and Brodd[38] shows that the numerically obtained values are in good agreement with the expected specific energy density and power density ranges of LIBs.

© 2020 The Authors. Energy Technology published by Wiley-VCH GmbH

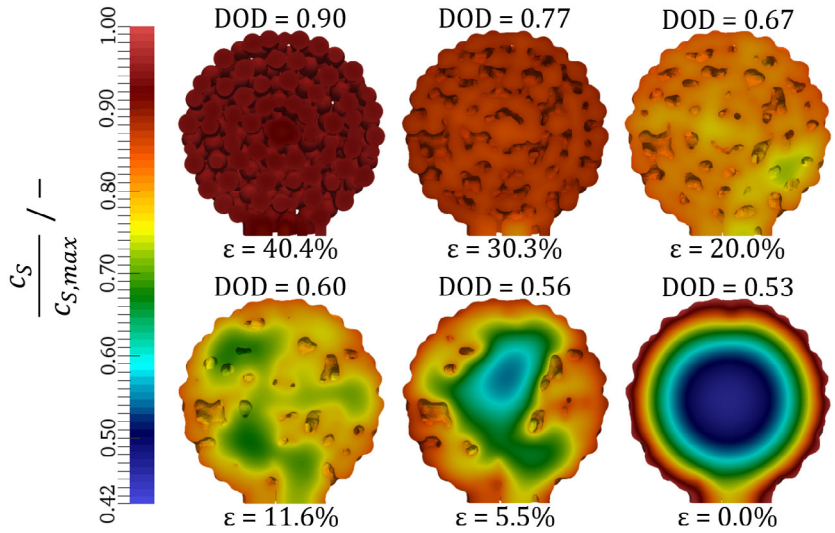

Figure 6. Simulation results for SAICs and same discharge times of 480 s of the investigated particles. The nonporous particle with a 4C discharge rate serves as a discharge current reference.

These two diagrams (a) and (b) can be interpreted as a summary of the conducted simulations in this contribution. Here, for each investigated particle, a number of discharge rates have been simulated, ranging from lowest applied discharge rate of 0.1C, over 0.5C, 1C, 4C and the SAIC as the nonporous reference particle with 4C, up to a discharge rate of 10C. The connecting lines between the respective data points serve the eye as an orientation guide along the results for the different porosities considered.

Figure 7a shows the volumetric interpretation of the results by considering identical numbers of AM particles. From the diagram, it can be seen that for the particles with a porosity $\varepsilon \geq 20\%$ at low C-rates, the UED is lower than for the less porous particles. For the case with $\varepsilon = 40.4\%$, its value is 37.8% lower compared to the nonporous particle at 0.1C. However, when the C-rate increases, the UED of the highly porous particles remain at an almost constant level. On the other hand, it can be seen that at decreasing inner porosities of the particles and increasing UPD, the UED decreases. The latter can be seen from the increasingly negative slopes of the guiding lines for decreasing porosities of the examined particles.

The behavior of the highly porous particles suggests that transport limitations are low. Furthermore, the low UEDs of the highly porous particles result from the low solid volumes, which result in a lower theoretical maximum capacity.

In addition, it can be seen in Figure 7a that at high UPDs $> 10\,\mathrm{Wm}^{-3}$, the particles with $20\% \leq \varepsilon \leq 30.3\%$ show a higher absolute UED than the particles with 5.5% and 0% porosity. This is despite the fact that the theoretical capacities of the two densest particles investigated are 18% and 25% higher, compared to the particle with a porosity of 20%. The reason for this is, that for the dense particles transport limitations at increasing C-rates become dominant, which macroscopically lead to lower UEDs of the respective particles.

Considering the values of the gravimetric results in Figure 7b, the attainable values of the UED at a given UPD increase with the porosity. Here, the most porous particle outperforms the particles with lower inner porosity for all simulated UPDs. The reasons for this are a high internal active surface area in combination with an open pore structure, which lower the transport resistances within particles with increasing inner porosity. Hence, the most porous particle shows the best utilization of the AM. However, it should be noted that when considering the same AM mass, a larger total volume of highly porous particles is required compared with the particles with lower porosities.

As discussed earlier, the assessment of an optimum particle porosity depends on several criteria. For the evaluation of this multi-criteria decision problem, the utility value (UV) analysis,[39] originating from the economical decision theory is applied. Within this method, the optimum lies in the maximum of the total utility value (TUV), which is calculated by the sum of the normalized and weighted UVs (see Equation (22)).[39]

$$\mathrm{TUV}(\varepsilon, \mathrm{C-rate}) = \sum_{i=1}^{k} \mathrm{g}_i \cdot \mathrm{UV}_i(\varepsilon, \mathrm{C-rate}) \tag{22}$$

The weighting factors g_i are used to emphasize the importance of the individual UVs and can take values between zero and one, while the sum of the weighting factors equals unity. As the respective UED and UPD are of interest for the decision to be made, these two values are used as UVs. They are either volumetrically or gravimetrically normalized to their specific maximum in each case scenario. Hence, the TUV is defined in the range between zero and unity. In the best case, the TUV reaches a value of one, which would be the case if the weighting factors were both nonzero and the maximum UED value and the maximum UPD value of the considered scenario coincide with one particular porosity.

In Figure 7c, the TUVs of the volumetric and in Figure 7d, the TUVs of the gravimetric approach of the investigated porous particles are shown. To be able to compare the results for the particle-related SAIC, the normalized values of UED and UPD with different weighting factors are depicted. The weighting factors of UED and UPD vary between the values zero and one in

© 2020 The Authors. Energy Technology published by Wiley-VCH GmbH

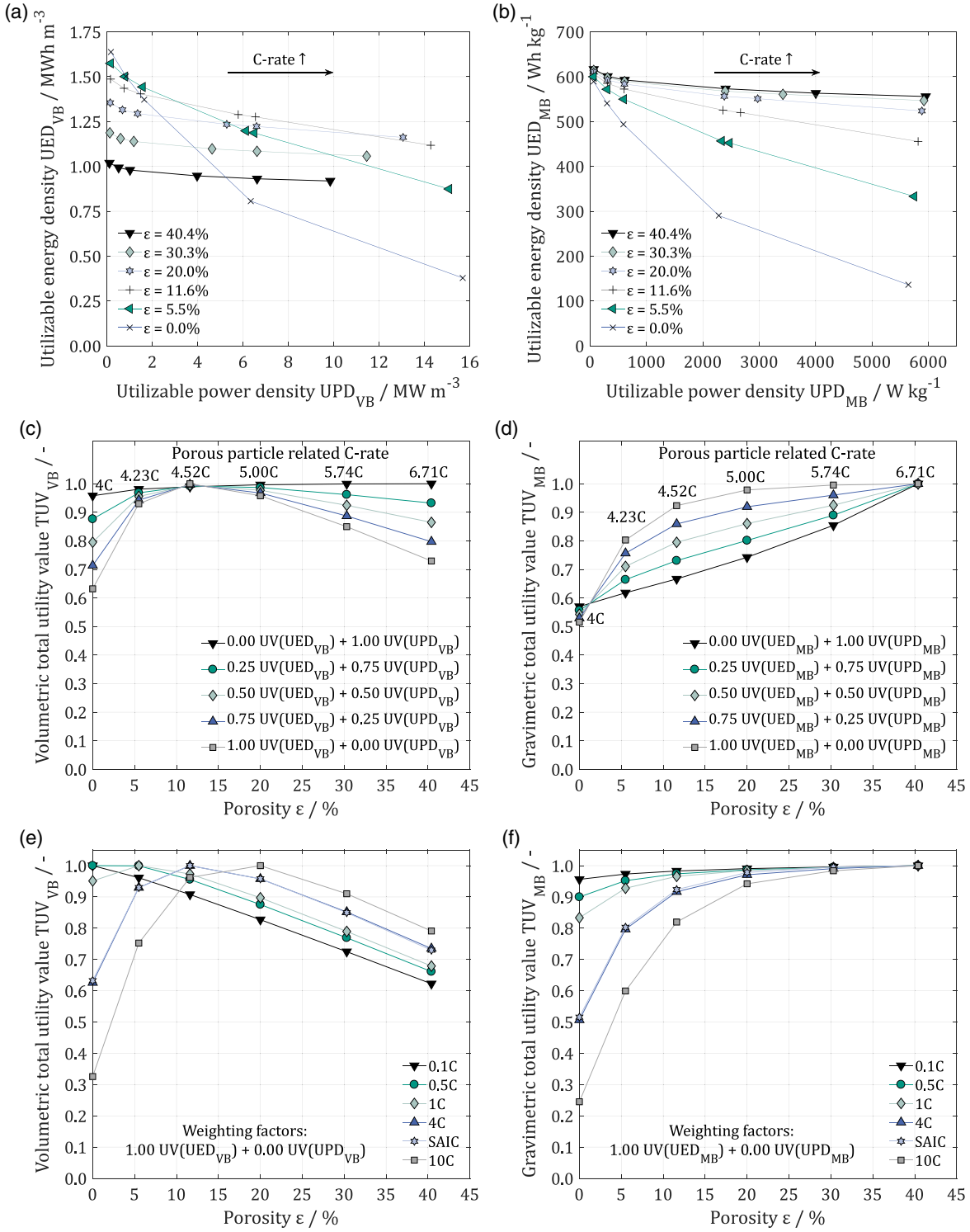

Figure 7. Diagrams based on Ragone plots of the a) volumetric (VB) and b) gravimetric (MB) results, as well as TUV plotted over the particle porosities in c,e) VB and d,f) MB results. The connecting lines serve as guidance for the eye and highlight in (a) and (b) the results for the same porosity. In (c) and (d), the TUV of the cases with SAIC and with identical weighting factors are connected. In (e) and (f), the TUV of the same C-rates are highlighted. As the weighting factor for UV(UED) is 1, only the normalized UEDs are shown.

steps of 0.25. The connecting lines serve as a guidance of the eye for the TUVs with identical weighting. As expected, the values of the mixed-weighted TUVs are between those of pure UED and pure UPD.

© 2020 The Authors. Energy Technology published by Wiley-VCH GmbH

In Figure 7c, it can be seen that the UV of the volumetric UPD is lower for cases with the SAIC at lower porosities $\varepsilon < 20\%$ (black triangle, e.g., $TUV_{VB}(\varepsilon = 0\%) = 0.96$ and $TUV_{VB}(\varepsilon = 11.6\%) = 0.99$). As the results are based on the same number of particles, the total current for each cubic meter of cathode paste is identical. The difference between the considered scenarios is that the smaller active surface area of the particles with low porosity leads to higher intercalation current densities, which facilitate a diffusion-limited state of operation. This in turn is reflected in a reduced half-cell potential. As the electrical power is the product of the electrical voltage and the electrical current, this leads to a reduced UPD.

It can be seen in Figure 7c that the particles with $\varepsilon > 20\%$ show a higher UPD compared to the denser counterparts, which is due to the lower transport resistances in these particle structures. However, the UED for the mentioned particles remains at lower values, as the capacity is already used up before a transport-limiting state of operation is reached. In case of the SAIC, the particle with an inner porosity of $\varepsilon = 11.6\%$ shows an optimum with respect to the TUV of the volumetric UED.

In Figure 7d, the gravimetric TUVs of the scenario with SAIC per particle are shown. From this diagram, it can be seen that the UVs for the pure UPD (black triangles) increase with increasing porosity. As the gravimetric approach considers the same mass of AM, the number of particles increases with increasing porosity. For this reason, the total current of the same mass of particles with $\varepsilon = 40.4\%$ is 1.68 times higher than that of the nonporous particles.

Looking at the UVs of the pure UED (gray squares), again the particles with the highest investigated internal porosity of $\varepsilon = 40.4\%$ show the optimum of the TUV. With decreasing porosity, this UV decreases nonlinearly and reaches for the nonporous particles 51.6% compared to the value of the same mass of particles with a porosity of $\varepsilon = 40.4\%$.

From the viewpoint of the gravimetric approach, the most porous particles ($\varepsilon = 40.4\%$) show the best performance for both evaluated UVs, UED and UPD.

Figure 7e,f depict the volumetric and gravimetric TUVs over the inner porosity of the investigated particles for the different load conditions, respectively. The connecting lines serve as a guidance for the eye and link the considered operation scenarios. To obtain a quantitative measure to assess the discharge performance, here the weighting factor for the UED is set to unity as it represents a temporal integral of the discharge process (see Equation (18)–(20)).

In Figure 7e, it can be seen that the optimum inner porosity of the particles increases with increasing C-rate. At low discharge rates, e.g., 0.1C, nonporous NMC particles are the best choice because they have the highest theoretical energy density and at low discharge rates there are almost no transport limitations. However, with an increasing C-rate, the optimum shifts to higher porosities, e.g., to $\varepsilon = 20\%$ at 10C.

Furthermore, Figure 7e can be used to visualize the beginning of a transport-limited state of operation. Without limitation, which is approximately the case at 0.1C, the UED decreases linearly with increasing particle porosity. At increasing C-rates, the curves run through a maximum of the TUV, e.g., at a discharge rate of 4C, the curve reaches its maximum at about $\varepsilon = 11.6\%$. The buckling of the curves at their respective maximum are an indication of beginning transport limitations, which is more pronounced with decreasing inner porosity of the particles. This is because a change in the slope of the interconnecting lines starting at high inner particle porosity values means a reduced UC for the given state of operation. As the full theoretic capacity can be reached only at equilibrium conditions, a reduction of the UC is related to deviations from the equilibrium state and gets ever lower with increasing transport limitations, as it is the case for solid-state diffusion limitation.

In addition to that it can be seen in Figure 7e that in the range between $30.3\% < \varepsilon < 40.4\%$, the slope of the 10C-line is identical to the slopes of the lower discharge rates. Hence, according to the numerical results, at these inner particle porosities transport processes are still not a limiting factor. Therefore, it can be stated that these highly porous particles can be operated with C-rates higher than 10C while the UC remains at a high level. With further increasing C-rates, the volumetric optimum porosity is likely to shift to ever-higher porosities.

In the literature, it can be found that researchers[16–20] used nanotechnology to create various 3D AM structures, with a high porosity of up to 74% and an AM layer thickness of 30 nm to 200 nm. The results showed a high rate capability, in some cases of more than 1000C while maintaining 38% of the capacity within lithium-ion microbattery applications.[16–20]

The reason for that is that highly porous AM facilitates the lithium transport within the particles and structures due to small solid-state diffusion lengths and fast ion transport to the inner part of the AM through the electrolyte in the pores. This at the same time lowers the effective transport resistances and enables the material to withstand significantly higher discharge rates.

The simulation results reveal that the volumetric UED of the particle with $\varepsilon = 20\%$ exceeds the UED of the particles with lower inner porosity at 10C. This is counterintuitive as the particles with higher solid volume have a higher theoretic capacity. Hence, from the viewpoint of the volumetric approach, the NMC particle with an inner porosity of 20% performs best at 10C.

From the viewpoint of the gravimetric approach, see Figure 7f, the battery performance increases with an increasing inner porosity of the AM particles. Due to the large active surface area, lithium can be intercalated more homogeneously from the electrolyte. As a result, local intercalation current densities at a given C-rate are reduced, which lead to decreased local overpotentials. Furthermore, it could be shown in Figure 5 and 6 that concentration differences between the particle surface and the bulk of the particle are lower. This is due to decreased diffusion lengths, which lead to a reduction of solid-state diffusion limitation. Hence, the amount of intercalated lithium in the AM particles increases, even at high currents. In contrast, due to increasing solid-state transport limitations in particles with low porosity at increasing discharge currents, the UC of these particles decreases.

The presented numerical results are in good agreement with the results of the numerical study by Lueth et al.[24] They observed that pores inside AM particles reduce the total transport losses, while the additional active surface area reduces the charge transfer resistance. In their study, the calculated discharge capacities were higher for porous particles and this effect was

© 2020 The Authors. Energy Technology published by Wiley-VCH GmbH

more pronounced at higher C rates. In addition to that, the experimental study by Dreizler et al.[23] highlights the positive effect of the porous AM particles. They found that cells made from porous AM had a higher UC compared to reference cells made from nonporous AM. They attributed this to a reduced internal cell resistance and, as a consequence, a lower potential drop under load conditions. Furthermore, they observed that the number of charge–discharge cycles in long-term tests was always higher for the nanostructured electrodes, regardless of the electrode thickness. For this reason, they considered porous particles as advantageous especially for high-performance applications and that those can contribute to an elongated battery cycle life.

In summary, it can be stated that the porosity of the AM particles directly influences the electrochemical performance and the optimal internal particle porosity depends on the intended application. In case of a limited total battery volume, nonporous particles perform best in high-energy, but low-current applications. In medium to high power applications, with discharge rates between 1C and 10C, particle porosities between 10% and 20% perform best in terms of the volumetric UED. If the battery volume is unlimited, as is usually the case in stationary applications, the highly porous particles with over 40% porosity show the best gravimetric performance. Therefore, it always depends on the desired application whether a high UED or UPD should be achieved and the appropriate particle porosity can be selected accordingly.

5. Conclusion and Outlook

In this contribution, spatially resolved simulations of single, differently porous NMC particles are conducted to investigate the influence of the inner AM porosity on the electrochemical performance. To ensure comparability of the numerical results, computer-generated porous particles with identical primary particle arrangements are used. The inner porosity is adjusted by means of varying the thickness of the sintering bridges. To investigate the electrochemical performance, a numerical C-rate study is carried out. For the evaluation of the results, volumetric and gravimetric approaches are used and a UV analysis is performed, to find the optimum porosity.

The findings of the investigations are that the inner porosity of the AM particles increasingly affects the electrochemical performance at higher discharge rates. At low discharge rates, a high UED is related to a high solid volume, which makes dense particles more favorable. At increasing C-rates, higher inner particle porosities with an open pore-structure become more and more advantageous, because the transport of lithium ions through the electrolyte is faster, compared to the solid-state diffusion in NMC. Hence, less effective transport resistances occur. Furthermore, the active surface area rises with increasing porosity, so that the local intercalation current densities decrease. This in turn leads to lower local overpotentials, so that higher UCs can be reached. The downside of increasing inner particle porosities, however, is the decreasing theoretical per-particle capacity for a given particle size.

However, inner porosities $<20\%$ are found to be disadvantageous for two reasons. On the one hand, at small pore cross-sections, increased ionic current densities in the electrolyte can occur, especially if they serve as a connector to a large inner surface area of closed pores. Hence, these areas are prone to become hot spots and promote electrolyte depletion. On the other hand, closed pores lead to increased diffusion lengths inside the solid phase of the particles, so that solid-state diffusion limitation becomes more dominant.

Summarizing the results, it can be stated that the optimum inner particle porosity depends on the intended field of application. Considering a limited available battery volume in high-energy applications with low currents, nonporous particles perform best. In medium to high power applications, with discharge rates between 1C and 10C, porosities between 10% and 20% show the highest UEDs. If the battery volume is not a limiting factor, e.g., in stationary applications, particles with a maximum inner porosity show the best AM utilization and gravimetric high-power capability. An UV analysis, as presented in this contribution, has the potential to assist in selecting the appropriate particle porosity for the desired application.

To what extent the presented results of the single secondary particle simulations can be transferred to representative electrode microstructures is subject of ongoing research.

Acknowledgements

The authors thank Benjamin Radel, Felix Gerbig, and Amadeus Wolf for the many fruitful discussions. Furthermore, funding and support by the German Research Foundation (Deutsche Forschungsgemeinschaft [DFG]) within the research training group SiMET under the project number 281041241/GRK2218 are gratefully acknowledged. Moreover, the authors acknowledge support by the Ministry of Science, Research and Arts Baden-Wuerttemberg and by the Federal Ministry of Education and Research through funding of ForHLR supercomputer. Open access funding enabled and organized by Projekt DEAL.

Conflict of Interest

The authors declare no conflict of interest.

Keywords

electrochemical performances, inner particle porosity, optimum energy and power density, particle morphology, positive electrodes, three-dimensional battery simulations

Received: July 21, 2020
Revised: October 12, 2020
Published online:

[1] a) G. E. Blomgren, *J. Electrochem. Soc.* **2017**, *164*, A5019; b) M. V. Corazza, U. Guida, A. Musso, M. Tozzi, *Transp. Res. Part D* **2016**, *45*, 48; c) J.-M. Tarascon, *Philos. Trans. Ser. A* **2010**, *368*, 3227.
[2] *Materials for Sustainable Energy. A Collection of Peer-Reviewed Research and Review Articles from Nature Publishing Group* (Eds.: J.-M. Tarascon, M. Grätzel, V. Dusastre), Nature Publising Group, Hackensack, NJ **2011**.
[3] N. Nitta, F. Wu, J. T. Lee, G. Yushin, *Mater. Today* **2015**, *18*, 252.
[4] *Handbuch Lithium-Ionen-Batterien* (Ed. R. Korthauer), Springer Berlin Heidelberg, Berlin, Heidelberg **2013**.

© 2020 The Authors. Energy Technology published by Wiley-VCH GmbH

[5] A. H. Wiedemann, G. M. Goldin, S. A. Barnett, H. Zhu, R. J. Kee, *Electrochim. Acta* **2013**, *88*, 580.
[6] R. E. García, Y.-M. Chiang, W. Craig Carter, P. Limthongkul, C. M. Bishop, *Chem. Mater.* **2005**, *152*, A255.
[7] a) R. E. García, Y.-M. Chiang, *J. Electrochem. Soc.* **2007**, *154*, A856; b) G. M. Goldin, A. M. Colclasure, A. H. Wiedemann, R. J. Kee, *Electrochim. Acta* **2012**, *64*, 118; c) W. Mai, M. Yang, S. Soghrati, *Electrochim. Acta* **2019**, *294*, 192; d) A. N. Mistry, K. Smith, P. P. Mukherjee, *ACS Appl. Mater. Interfaces* **2018**, *10*, 6317; e) A. Rucci, A. C. Ngandjong, E. N. Primo, M. Maiza, A. A. Franco, *Electrochim. Acta* **2019**, *312*, 168; f) M. Kespe, H. Nirschl, *Int. J. Energy Res.* **2015**, *39*, 2062.
[8] G. B. Less, J. H. Seo, S. Han, A. M. Sastry, J. Zausch, A. Latz, S. Schmidt, C. Wieser, D. Kehrwald, S. Fell, *J. Electrochem. Soc.* **2012**, *159*, A697.
[9] M. Kespe, M. Gleiß, S. Hammerich, H. Nirschl, *Int. J. Energy Res.* **2017**, *41*, 2282.
[10] M. Kespe, S. Cernak, M. Gleiß, S. Hammerich, H. Nirschl, *Int. J. Energy Res.* **2019**, *43*, 6762.
[11] a) T. Hutzenlaub, S. Thiele, N. Paust, R. Spotnitz, R. Zengerle, C. Walchshofer, *Electrochim. Acta* **2014**, *115*, 131; b) S. A. Roberts, V. E. Brunini, K. N. Long, A. M. Grillet, *J. Electrochem. Soc.* **2014**, *161*, F3052; c) S. A. Roberts, H. Mendoza, V. E. Brunini, B. L. Trembacki, D. R. Noble, A. M. Grillet, *J. Electrochem. Energy Conv. Storage* **2016**, *13*, 178.
[12] A. Latz, J. Zausch, *Beilstein J. Nanotechnol.* **2015**, *6*, 987.
[13] X. Xu, S. Lee, S. Jeong, Y. Kim, J. Cho, *Mater. Today* **2013**, *16*, 487.
[14] C. Julien, A. Mauger, K. Zaghib, H. Groult, *Materials* **2016**, *9*, 595.
[15] M.-J. Uddin, P. K. Alaboina, S.-J. Cho, *Mater. Today Energy* **2017**, *5*, 138.
[16] H. Zhang, X. Yu, P. V. Braun, *Nat. Nanotechnol.* **2011**, *6*, 277.
[17] W. Tang, X. J. Wang, Y. Y. Hou, L. L. Li, H. Sun, Y. S. Zhu, Y. Bai, Y. P. Wu, K. Zhu, T. van Ree, *J. Power Sources* **2012**, *198*, 308.
[18] J. H. Pikul, H. Gang Zhang, J. Cho, P. V. Braun, W. P. King, *Nat. Commun.* **2013**, *4*, 1732.
[19] H. Ning, J. H. Pikul, R. Zhang, X. Li, S. Xu, J. Wang, J. A. Rogers, W. P. King, P. V. Braun, *Proc. Natl. Acad. Sci. U. S. A.* **2015**, *112*, 6573.
[20] Z. Ding, J. Liu, R. Ji, X. Zeng, S. Yang, A. Pan, D. G. Ivey, W. Wei, *J. Power Sources* **2016**, *329*, 297.
[21] Z. Liu, X. Yuan, S. Zhang, J. Wang, Q. Huang, N. Yu, Y. Zhu, L. Fu, F. Wang, Y. Chen Y. Wu, *NPG Asia Mater.* **2019**, *11*, 16023.
[22] K. M. Shaju, P. G. Bruce, *Adv. Mater.* **2006**, *18*, 2330.
[23] A. M. Dreizler, N. Bohn, H. Geßwein, M. Müller, J. R. Binder, N. Wagner, K. A. Friedrich, *J. Electrochem. Soc.* **2018**, *165*, A273.
[24] S. Lueth, U. S. Sauter, W. G. Bessler, *J. Electrochem. Soc.* **2016**, *163*, A210.
[25] S. Cernak, F. Gerbig, M. Kespe, H. Nirschl, *Energy Storage* **2020**, e156.
[26] V. Wenzel, H. Nirschl, D. Nötzel, *Energy Technol.* **2015**, *3*, 692.
[27] J. A. Gilbert, I. A. Shkrob, D. P. Abraham, *J. Electrochem. Soc.* **2017**, *164*, A389.
[28] M. Ebner, F. Geldmacher, F. Marone, M. Stampanoni, V. Wood, *Adv. Energy Mater.* **2013**, *3*, 845.
[29] R. Marques, C. Bouville, M. Ribardière, L. P. Santos, K. Bouatouch, *Comput. Graph. Forum* **2013**, *32*, 134.
[30] J. Newman, K. E. Thomas-Alyea, *Electrochemical Systems*, 3rd ed., Wiley-Interscience, New York **2012**.
[31] A. Latz, J. Zausch, *J. Power Sources* **2011**, *196*, 3296.
[32] S. G. Stewart, V. Srinivasan, J. Newman, *J. Electrochem. Soc.* **2008**, *155*, A664.
[33] F. M. Kindermann, A. Noel, S. V. Erhard, A. Jossen, *Electrochim. Acta* **2015**, *185*, 107.
[34] E. Bohn, T. Eckl, M. Kamlah, R. McMeeking, *J. Electrochem. Soc.* **2013**, *160*, A1638.
[35] J. Landesfeind, J. Hattendorff, A. Ehrl, W. A. Wall, H. A. Gasteiger, *J. Electrochem. Soc.* **2016**, *163*, A1373.
[36] D. P. Abraham, J. L. Knuth, D. W. Dees, I. Bloom, J. P. Christophersen, *J. Power Sources* **2007**, *170*, 465.
[37] D. V. Ragone, in *SAE Technical Paper Series*, SAE International, Warrendale, PA **1968**.
[38] M. Winter, R. J. Brodd, *Chem. Rev.* **2004**, *104*, 4245.
[39] G. Bamberg, A. G. Coenenberg, M. Krapp, *Betriebswirtschaftliche Entscheidungslehre*, Verlag Franz Vahlen GmbH, München **2019**.
[40] K. Smith, C.-Y. Wang, *J. Power Sources* **2006**, *161*, 628.
[41] S. Cui, Y. Wei, T. Liu, W. Deng, Z. Hu, Y. Su, H. Li, M. Li, H. Guo, Y. Duan, W. Wang, M. Rao, J. Zheng, X. Wang, *Adv. Energy Mater.* **2016**, *6*, 1501309.
[42] C. Xing, M. Zhao, L. Zhao, J. You, X. Cao, Y. Li, *Polym. Chem.* **2013**, *4*, 5726.
[43] M. Wood, J. Li, R. E. Ruther, Z. Du, E. C. Self, H. M. Meyer, C. Daniel, I. Belharouak, D. L. Wood, *Energy Storage Mater.* **2020**, *24*, 188.
[44] S. Tippmann, D. Walper, L. Balboa, B. Spier, W. G. Bessler, *J. Power Sources* **2014**, *252*, 305.
[45] M. Doyle, T. F. Fuller, J. Newman, *J. Electrochem. Soc.* **1993**, *140*, 1526.

© 2020 The Authors. Energy Technology published by Wiley-VCH GmbH